Article:

eprints@whiterose.ac.uk
https://eprints.whiterose.ac.uk/

Dynamic modelling of wind turbine gearbox bearing loading during transient events

T. Bruce, H. Long*, R. S. Dwyer-Joyce

Leonardo Centre for Tribology, Department of Mechanical Engineering, The University of Sheffield, United Kingdom

*h.long@sheffield.ac.uk
Tel: +44 (0) 114 222 7759
Fax: +44 (0) 114 222 7890

Abstract

Wind turbine gearbox bearings (WTGBs) are the most reliability critical component in wind turbine gearboxes (WTGs) due to their high failure rate and long downtime-per-failure. Current design methods predict bearing failure by fatigue life models. However, premature WTGB failures have been observed by many other modes. This study presents the development of a multibody dynamic gearbox model, used to determine maximum bearing contact stresses from laboratory measured shaft torque data during normal operation and shutdown conditions. The model was validated by comparing its results to other models of the 750 kW National Renewable Energy Laboratory (NREL) test drive train by the Gearbox Reliability Collaborative (GRC). During normal operation, the maximum contact stress experienced by the planetary stage bearings exceeded recommended levels by 1% and during shutdown, by 15%. High speed shaft bearings also exceeded recommended levels during shutdown, by 18%.

Keywords

Wind turbine gearbox, bearing failure, multibody, dynamic model, overload, white etching crack.

1. Introduction

Approximately two-thirds of WTG failures initiate in the bearings [1] despite best practice manufacturing being followed [2]. A typical onshore failure takes around 250 hours to repair and 20% of the overall lifetime downtime of a wind turbine (WT) can be expected to be caused by gearbox failures [3], with this percentage greatly increased for offshore applications. Current standards explain bearing failure via rolling contact fatigue [4], but do not explain the shortened lifetimes. It is clear that the bearing failures have other root causes [3, 5].

The number of failures increases with WT size, due to larger component deflections and misalignment [5, 6]; although NREL found that size does not affect the mode of failure [7]. European offshore wind capacity is expected to increase by approximately 30-40 times 2011 levels by 2020 [8], with offshore WTs being more expensive to repair than onshore.

The purpose of the model developed in this study is to determine whether maximum bearing contact pressures are exceeding recommended levels during normal operation and manual shutdown conditions. A dynamic gearbox model of the NREL two-speed, stall-regulated 750 kW test drivetrain was created, using Ricardo PLC*'s VALDYN* software. The model was then validated against models of the same gearbox, created independently by the NREL GRC round-robin project. Simulation results of bearing dynamic loading are presented and maximum Hertzian contact stresses calculated.

2. Review of Recent Research

2.1. Causes of premature failure in wind turbine gearbox bearings

Overloading may be a cause of premature failure [9], occurring when the contact pressure between a bearing raceway and rolling element is higher than the material's yield strength. Overloading is caused by short-term impact loading, which may arise from: fluctuating wind loads, non-synchronisation of blade pitch (for machines with pitching blades), sudden braking, sudden grid drops, generator/grid engagements [9], extended periods of high rotor torque, misalignment due to gearbox component deflections, oval compression of gearbox bearings due to gearbox support structure deflections, oval compression of blade pitch bearings causing short term torque spikes due to

delayed blade pitching [10], non-torsional loading [11], preloading on account of tight fits, excessive drive-up on a tapered seating, extreme events leading to torque reversal (for example emergency shutdown), or impact during fitting [12, 13]. When rolling elements are in the unloaded zone, they can be instantaneously loaded beyond the material's yield strength in misaligned conditions, along one or two contact points in the load profile [9]. These periods of heavy, dynamic loading may lead to raceway stresses exceeding 3.1 GPa [10].

Possible damage modes may include, subsurface damaged due to localised adiabatic heating [14], or if impact loads are high enough to cause low cycle fatigue, failure may occur over a relatively low number of load cycles [15]. Overloading may lead to the development of hard, brittle, white etching cracks (WECs) [9, 13]. Repetitive impact loading (hammering impact), may occur during torque reversals, leading to many overload cycles in a short time period. If WECs propagate to the raceway surface, they may initiate failure by spalling [9] or axial cracking [16]; a mode of damage that can lead to bearing failure within 1-20% of the L_{10} design life [17]. These observations indicate overloading over short time periods is a potential cause of the premature bearing failure, validating the need to model a WTG during transient loading.

2.2. Dynamic system modelling

Peeters et al. [18] compared three types of WTG model.

- 1: Torsional multibody models, modelled with 1 degree of freedom (DOF);

- 2: Six DOF rigid multibody models with discrete flexible elements;

- 3: Fully flexible multibody models.

Type 1 models are useful for modelling drivetrains during the early design stage, and are suitable for investigating dynamic torque levels, but not for modelling bearing reaction forces [19]. A study of a type 1 gearbox model used to simulate normal operation and emergency stop conditions found that most off-axis wind loads are absorbed by the main rotor shaft bearings before entering the gearbox [1], a finding supported by NREL [20]. Failure-by-fatigue analysis [4] was used to conclude that the first stage planetary bearings showed the greatest amount of fatigue damage, which was within acceptable limits. Normal stops caused no additional damage but emergency stops led to higher

damage levels, especially immediately after grid loss. The model did not predict any excess loads on the HSS (High Speed Shaft) [1].

Type 2 models can be used to investigate the influence of bearing stiffness on drivetrain dynamics [18] and to model planetary and parallel stages as well as complete gearboxes [19]. It is useful to use a 'sliced' model for gear tooth contact [21], dividing it into many 'spring-damper' force elements. Axial forces introduced by helical gears can be well modelled using this method, which is important due to the induced moment on the planet gears, leading to shaft bending and misalignment. A 35-slice contact model was determined to be the optimum compromise between accuracy and computational cost [21].

Type 3 models are able to calculate internal component stresses and strains, but with high computational expense [18, 19]. The computational cost of each model type was investigated [20, 21] by developing a gearbox model, initially as a two mass system (rotor and generator), and incrementally increasing its complexity, validating each stage against a tested braking event. Type 2 model cost was 400 % higher than type 1, with type 3 a further 26 % higher than type 2. It was found that type 1 models are time effective and that accurate modelling is possible using type 2, without using finite element analysis. A new method of multibody dynamic modelling, streamlined for efficiently calculating bearing loading, has been developed in this study, using the software package "VALDYN".

3. Development of a dynamic WTG model using VALDYN

The proposed new model is compared to existing models in Table 1 and is described as modified type 2. It is able to model variable bearing stiffness, bearing damping and uses a sliced gear mesh stiffness model.

Modelled stiffness	Type 1 – 1 DOF torsional model	Type 2 – 6 DOF rigid multibody model	Type 3 – Flexible multibody model	Proposed model in this study
Gear mesh	Constant	Constant	Variable	Constant (sliced model)
Bearing	Rigid	Constant axial, radial, tilt (no damping)	Variable axial, radial, tilt (stiffness and damping)	Variable axial, radial, tilt (stiffness), constant damping
Shaft	Discrete torsional	Discrete torsional,	FEA representation	Discrete torsional,

		Equivalent bending		Equivalent bending
Splined connection	Torsional spline connection	Torsional spline connection	Discrete torsional, Discrete bending, Discrete tilting	Torsional spline connection
Structural components	Rigid	Rigid	FEA representation	Rigid
Outputs				
Torque time history	✓	✓	✓	✓
Detailed reaction forces		✓	✓	✓
Internal stresses and strains			✓	✓ (bearings only)

Table 1: Comparison of model types 1-3 to proposed gearbox model (adapted from [19])

Figure 1a shows a conventional WT drivetrain and the coordinate system used in this study. All components were modelled, with the exception of the bedplate, which was assumed to be rigid, and the main shaft bearings, as it was assumed that no off-axis wind loads were transmitted to the gearbox, an accepted assumption [1, 21]. Gearbox components were modelled in 6 DOFs, while the rotor and the generator were modelled as point inertias, free to rotate in the Z′ direction. A typical WTG is shown schematically in Figure 1b including the description of the bearings used in the developed model. VALDYN was used to dynamically model all components at each timestep using the equation of motion (1), where [M], [C], and [K] are the inertia, damping and stiffness matrices representing the modelled components respectively; $\{\ddot{X}\}, \{\dot{X}\}$ and $\{X\}$ represent the acceleration, velocity and displacement of each modelled component respectively and {F} represents the calculated forces and moments bearing supports. These matrices are described in more detail in equations (2-19). All required input parameters are listed in Table 5 in the appendix.

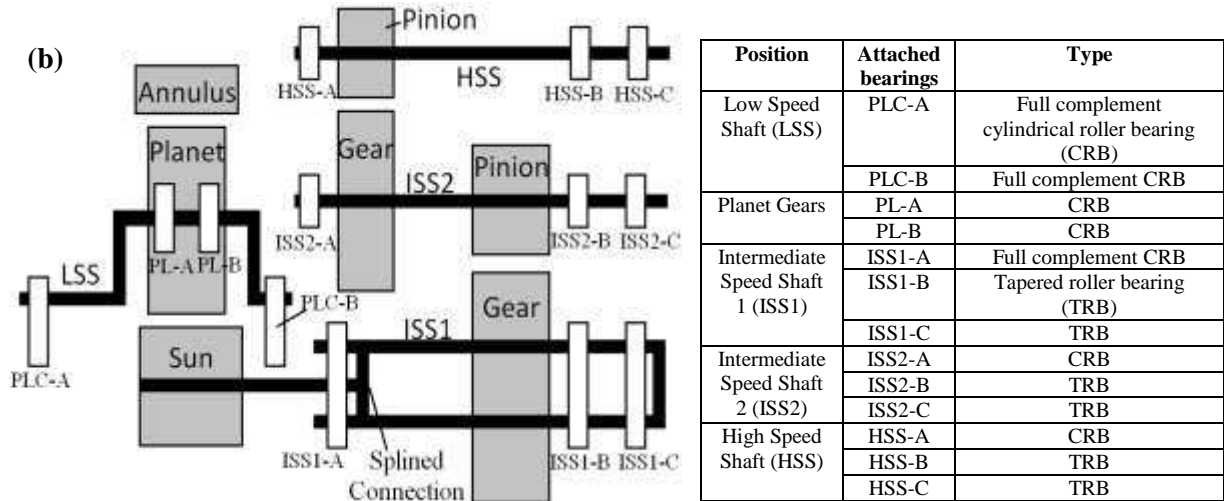$$[M]\{\ddot{X}\} + [C]\{\dot{X}\} + [K]\{X\} = \{F\} \qquad (1)$$

(a) Hub, Main Bearing, Main Shaft, Main Bearing, Gearbox, Brake Disc, High-Speed Shaft, Generator, Bedplate

Position	Attached bearings	Type
Low Speed Shaft (LSS)	PLC-A	Full complement cylindrical roller bearing (CRB)
	PLC-B	Full complement CRB
Planet Gears	PL-A	CRB
	PL-B	CRB
Intermediate Speed Shaft 1 (ISS1)	ISS1-A	Full complement CRB
	ISS1-B	Tapered roller bearing (TRB)
	ISS1-C	TRB
Intermediate Speed Shaft 2 (ISS2)	ISS2-A	CRB
	ISS2-B	TRB
	ISS2-C	TRB
High Speed Shaft (HSS)	HSS-A	CRB
	HSS-B	TRB
	HSS-C	TRB

Figure 1: NREL gearbox layout: (a) Typical WT drivetrain configuration and coordinate system (b) Gearbox schematic [7]

3.1. Mass and inertias of gearbox components

The mass matrix below describes the mass and inertia of each component, where M is its mass and $I_{X'}$, $I_{Y'}$ and $I_{Z'}$ are its inertia in the X′, Y′ and Z′ directions respectively. Masses and inertias were found from component data sheets where possible, or alternatively, using CAD models.

$$
\begin{vmatrix}
M & 0 & 0 & 0 & 0 & 0 \\
0 & M & 0 & 0 & 0 & 0 \\
0 & 0 & M & 0 & 0 & 0 \\
0 & 0 & 0 & I_{X'} & 0 & 0 \\
0 & 0 & 0 & 0 & I_{Y'} & 0 \\
0 & 0 & 0 & 0 & 0 & I_{Z'}
\end{vmatrix}
\tag{2}
$$

3.2. Bearings

Bearing stiffness is described by the matrix shown below [22], where the value for $k_{Z'Z'}$ is zero, because this is the DOF representing rotation around the shaft axis (axial friction is considered later). Constant diagonal terms (shown in bold) assume linearly varying stiffness with bearing displacement [18]. The modified model in this study calculated varying stiffness terms from the inputted bearing geometry, taking into account the off-diagonal terms, which link the 6 DOFs. VALDYN is able to model both cylindrical roller bearings (CRBs) and tapered roller bearings (TRBs) in this way, using the theory presented in [23].

$$
\begin{vmatrix}
\mathbf{k_{XX}} & k_{XY} & k_{XZ} & k_{XX'} & k_{XY'} & 0 \\
 & \mathbf{k_{YY}} & k_{YZ} & k_{YX'} & k_{YY'} & 0 \\
 & & \mathbf{k_{ZZ}} & k_{ZX'} & k_{ZY'} & 0 \\
 & & & \mathbf{k_{X'X'}} & k_{X'Y'} & 0 \\
 & \text{Symmetric} & & & k_{Y'Y'} & 0 \\
 & & & & & \mathbf{k_{Z'Z'}}
\end{vmatrix}
\tag{3}
$$

The bearing loads, F_x, F_y and F_z, and tilting moments, M_x and M_y, are computed at each timestep as functions of the relative displacements x, y, z, x′, y′ of the outer and inner raceways, i and j respectively. Initial displacements must be zero. o_i and o_j are the initial axial inner and outer race offsets; the distance from the common centre of mass of the outer race and inner race respectively in the z direction [24]:

$$d_X = x_i - x_j \tag{4}$$

$$d_Y = y_i - y_j \tag{5}$$

$$d_Z = (z_i + o_i) - (z_j + o_j) \tag{6}$$

$$d_{X'} = x'_i - x'_j \tag{7}$$

$$d_{Y'} = y'_i - y'_j \tag{8}$$

Acceleration and velocity are calculated at each timestep, using these displacement results. VALDYN then calculates the forces, F_x and F_y, in the X and Y directions respectively and R_I, the radius at which the force acts. The loads F and moments M acting on each of the raceways are calculated in the following form [24]:

$$F_i = (F_x, F_y, F_z) \tag{9}$$

$$F_j = -F_i \tag{10}$$

$$M_i = \left((M_x - F_y \cdot o_i), (M_y + F_x \cdot o_i), M_z \right) \tag{11}$$

$$M_j = \left(-(M_x - F_y \cdot o_j), -(M_y + F_x \cdot o_j), -M_z \right) \tag{12}$$

The axial moment caused by bearing friction is calculated below, considering the coefficient of rotational friction μ. Assumed values of μ are 0.0011 and 0.0018 for CRBs and TRBs respectively [25].

$$M_z = \pm \mu R_I \sqrt{F_x{}^2 + F_y{}^2} \tag{13}$$

The most difficult bearing parameter to estimate accurately is its damping coefficient c. One method is to consider bearing damping as a fraction of its critical damping; calculated using equation 14 where k is the bearing stiffness and I is the inertia of the rolling elements [11].

$$c = 2\sqrt{Ik} \tag{14}$$

Introducing the ratio of the critical damping ζ allowed the level of the damping to be set.

$$c = 2\zeta\sqrt{Ik} \tag{15}$$

Bearing stiffness values at rated torque were used to calculate constant damping coefficients in the five restrained DOFs. Three damping coefficients were required; axial c_a, radial c_r and tilt c_t. Axial damping was calculated using the axial stiffness; radial damping, using the mean radial stiffness in the x and y directions; and tilt damping, using the mean tilt stiffness in the X′ and Y′ directions. Combining these damping values found using in equations (16-18) creating the damping matrix (19).

$$c_a = 2\zeta\sqrt{Ik_{zz}} \tag{16}$$

$$c_r = 2\zeta\sqrt{I\left(\frac{k_{xx}+k_{yy}}{2}\right)} \tag{17}$$

$$c_t = 2\zeta\sqrt{I\left(\frac{k_{x\prime x\prime}+k_{y\prime y\prime}}{2}\right)} \tag{18}$$

$$\begin{vmatrix} c_r & 0 & 0 & 0 & 0 & 0 \\ 0 & c_r & 0 & 0 & 0 & 0 \\ 0 & 0 & c_a & 0 & 0 & 0 \\ 0 & 0 & 0 & c_t & 0 & 0 \\ 0 & 0 & 0 & 0 & c_t & 0 \\ 0 & 0 & 0 & 0 & 0 & 0 \end{vmatrix} \tag{19}$$

3.3. Gears

As previously discussed, a 'sliced' gear tooth contact model was used. The higher the number of slices, the more accurate the results are, but at computational cost. A previous study found that the optimum number of slices is 35 [22]. This study found this number to be a good compromise between computational cost and accuracy.

Tooth contact stiffness were assumed because the effective tooth stiffness of a pair of spur gears is relatively independent of the tooth and gear size when standard involute tooth profiles are used [26]. For spur gears, $c' = 14$ N/(mm.μm) and for helical gears (helix angle, $\beta = 20^{o}$): $c' = 13.1$ N/(mm.μm). These values were adjusted appropriately for different helix angles.

Damping was approximated, using an appropriate critical damping ratio in the same manner as in section 3.2. It was assumed that gear contact friction is zero, as it is anticipated that it will have little effect on bearing loading.

3.4. Shafts

Non-rigid shafts were modelled by specifying connected masses and inertias, as well as the shaft dimensions, mass matrix and bending and torsional damping. As the damping values of the shaft were unknown, they were approximated, again by using an appropriate value for the critical damping ratio.

3.5. Planetary carrier

The planetary carrier was assumed to be a rigid body as the computational cost of using an FE model was too high. This assumption is valid, provided that modelling unequal load sharing between upwind and downwind planetary bearings is not required. The magnitude of the sum of the upwind and downwind bearing reaction forces for each planetary gear will be correct. Previously calculated scaling factors for unequal load sharing are later introduced to approximate maximum load magnitudes.

3.6. Splined sun shaft connection

Many WT gearboxes use a splined shaft connection to allow the planetary stage sun gear to 'float'. A floating sun gear centres itself within its planets, encouraging load sharing. The splined

connection was modelled as a rigid connection in the X, Y, Z and Z′ DOFs, while the X′ and Y′ degrees of freedom were unrestrained, allowing the sun gear move up and down. As the sun gear's position is restrained by the three planets, it displacements in these directions are small, and the assumption is valid.

3.7. Gearbox casing and elastomer supports

The gearbox casing was modelled under the assumption that it is rigid, using a series of zero-mass "connection points" at each bearing location that are linked to a mass positioned at the centroid. The casing's movement was unrestrained and supported by two rubber mounts. The stiffness and damping values of these rubber mounts were assumed to be constant, which is an acceptable assumption as casing displacements are small [21].

3.8. Generator resistance torque

A simple induction generator model was used to model the generator resistance torque curve (Figure 2) that was accurate for most operation modes, although too simple to model the WT start-up control system [7]. Four inputs were required: synchronous generator speed (ω_{syn}), HSS rated speed, HSS Rated torque and pullout torque; given by the following equations, where PR is the pullout ratio (the ratio of pullout torque to HSS rated torque) [7]:
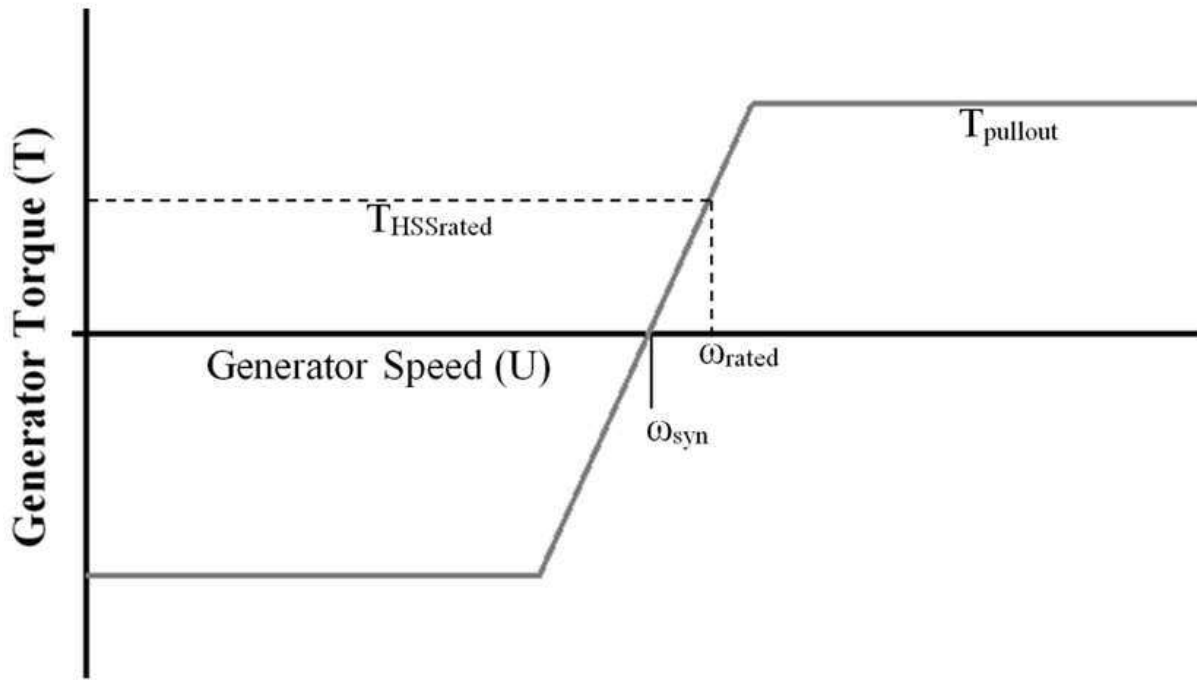
$$T_{pullout} = PR \times T_{HSSrated} \tag{20}$$

Figure 2: Generator resistance torque curve [7]

3.9. Disc braking

A trial and error process was utilised, by applying different contact loads (simulating the brake pads) to a brake disc, created using a braking element in VALDYN, which applied a frictional retarding force to the brake disc. Contact loads were altered until the time taken to bring the rotor to a stop from 10 rpm was the same as that taken for the tested event measured by NREL.

3.10. Maximum Hertzian contact stress calculation

After bearing dynamic loading was calculated, the maximum contact stress on the inner raceway of each bearing was calculated. First, the maximum load experienced by the most heavily loaded roller raceway contact Q_{max} was approximated using equation (21) [27], where P_{max} is the maximum load experienced perpendicular to the roller/raceway contact and z is the number of rolling elements. This calculation assumed that: the internal clearance of bearings was greater than zero, the elastic deformation of a rolling element was never negative, and the bearing roller was a perfect cylinder. These assumptions will lead to conservative bearing contact stress estimations as they do not take into account stress concentrations due to edge loading and roller profiling. Standard Hertzian calculations

for line contact loading (22) were used to calculate maximum contact pressure P_0, where a is the contact area [28].

$$Q_{max} = 5\frac{P_{max}}{z} \tag{21}$$

$$P_0 = 2\frac{Q_{max}}{\pi a} \tag{22}$$

4. Application to the NREL750 kW WTG

The NREL 750 kW gearbox, shown in Figure 2, was modelled in this study, which is a conventional three-stage design, with a low speed, three gear planetary stage, followed by two parallel stages. The gearbox ratio is 1:81.49, with a planetary stage ratio of 1:5.71, and two parallel ratios of 1:3.57 and 1:4.00 respectively. The sun gear is attached to the intermediate stage gear, via a shaft with a splined connection. The WT is able to generate power at two rated speeds, using either four or six generator poles.

As previously mentioned, it has been found that WTGB failures experienced by small-scale WTs (500-1000 kW) are also found in modern larger turbines. This confirms that findings from a study based on the 750 kW test-turbine, can be extrapolated to larger WTGs [7], despite their larger size, updated design standards and different control systems. This is highly advantageous because working with smaller turbine test facilities reduces cost and increases the availability of experimental research. Field and laboratory measurements are widely available for older turbines, whereas many modern designs are still protected by industry.

4.1. Model validation

The model was validated to evaluate the assumptions made during its development, against the results that were available for comparison. The first step was to compare torque distribution throughout the gearbox with that obtained by the anonymous GRC contributors involved in the round-

robin project [20]. The modelling method used by each of the partners involved different software packages, by which the studies were independently performed.

The VALDYN model was loaded at rated torque and the torque distribution throughout the gearbox was calculated and found to be very close to GRC results, as shown in Figure 3a. The maximum error from the mean result was 1.8% for the ISS2 torque level. The GRC mean result is possibly skewed by result D, which is slightly different from all other results. This comparison validates the model's torque distribution, proving that gearbox ratios and component dimensions have been setup correctly.

The loading levels in the sun/planet gear contact were tested to check the gear tooth contact model. The VALDYN model was run at rated torque until all vibrations caused by initial system unbalance had dissipated. Then the contact load was calculated and found to be very close to GRC results as shown in Figure 3b. The largest percentage difference from the mean GRC result was 2.4 % for the radial contact load. These slight differences are probably due to the use of different modelling methods.

Finally, the bending of the main shaft under rated load was checked to validate the assumptions used for modelling shaft bending and bearing stiffness. A model was created in which the shaft was split into four lengths, separated by five masses, with 6 DOF mass matrices representing the section of shaft they represented, allowing shaft deflection to be calculated in three locations between its supporting bearings. Main shaft bearing geometry, was input into the VALDYN model, which was loaded at rated rotor torque and the relative displacements of the main shaft was compared to NREL results. Figure 3c shows that the results from the GRC round-robin were inconsistent. Reading maximum displacement values from the figure allows the mean GRC result to be calculated to be approximately 7.3 μm. The calculated maximum value in this study; 8.2 μm, is around 11% higher than the mean magnitude and only the GRC result D is closer to this mean. This suggests that assumptions were reasonable and validates the method used to model shafts and their supports (bearing stiffness) in VALDYN.
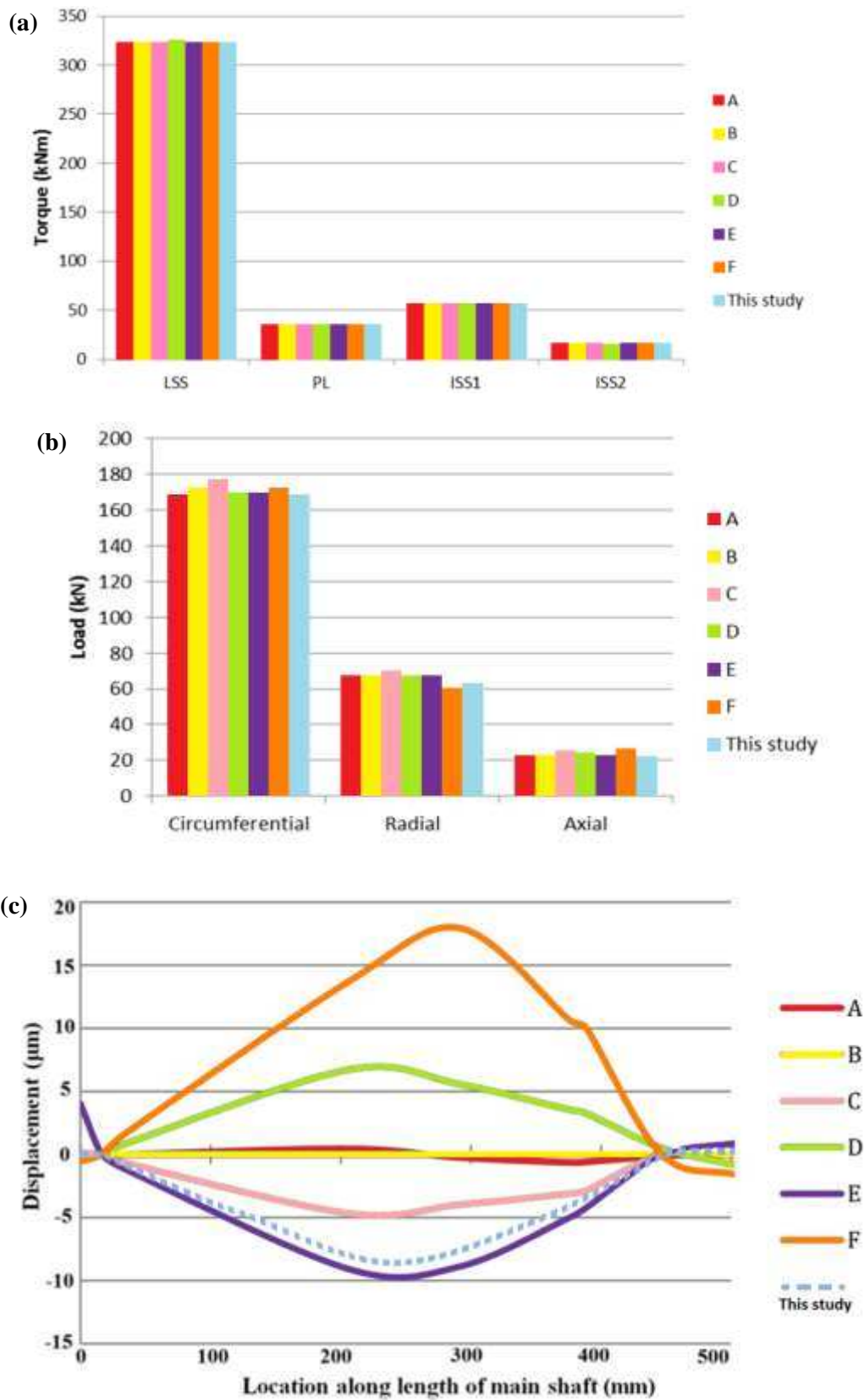
Figure 3: Validation of model in comparison to partners A-F (20) (a) Shaft torque levels (b) Planet-sun gear contact load levels (c) Main shaft bending displacement

4.2. Torque loading

Input torque and rotor speed data were provided by NREL for the following conditions:

- Normal Operation: 90 seconds of operation at six-pole rated speed.

- Shut-down: the rotor begins at six-pole rated speed, then the generator is disconnected and aerodynamic braking is initiated, until the rotor reaches 10 rpm, at which point the disc brake is engaged, bringing the rotor to a halt.

Figure 4 shows the input torque for the two operating conditions that were investigated by the developed multibody dynamic model.
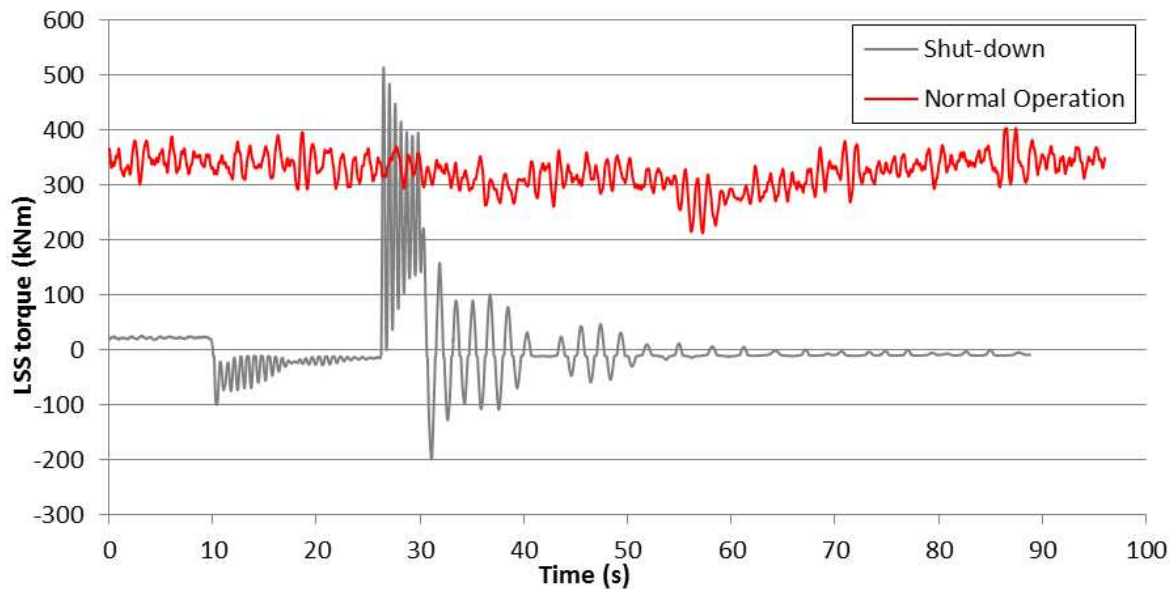

Figure 4: Input torque for normal operation and shutdown events

5. Results from simulated model and analysis

Planetary gear bearings and HSS bearings have historically been the most problematic in wind turbines, so were selected to be analysed in detail in this study.

5.1. Normal operation

Figure 5 displays the LSS and HSS velocities over the 96 second simulation period. Ignoring oscillations caused by initial system unbalance during the first 5 seconds, LSS speed oscillation magnitudes of approximately 0.8 rpm compare well with NREL measured data, and the average

velocity of the simulated LSS signal was 0.13% different from NREL measured data. No comparison

data was available for HSS velocity, which oscillates either side of the generator rated speed of 1809

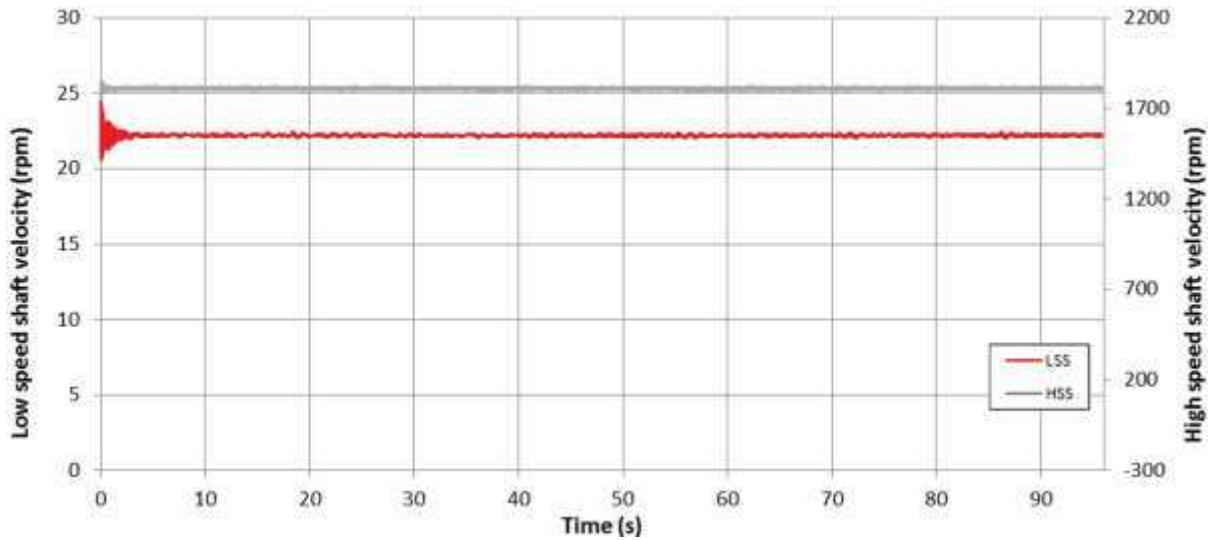rpm by approximately +/-5 rpm.

Figure 5: LSS and HSS velocity during normal operation

Figure 6a shows the resultant force acting on the planetary bearings, PL-A and PL-B, supporting

each planet gear. The maximum resultant force experienced was 280 kN. Figure 6b shows the

resultant forces acting on the HSS bearings, which in the case of HSS-B and HSS-C include both axial

and radial elements, as they are TRBs, with maximum values of 63 kN, 79 kN and 15 kN for HSS-A,
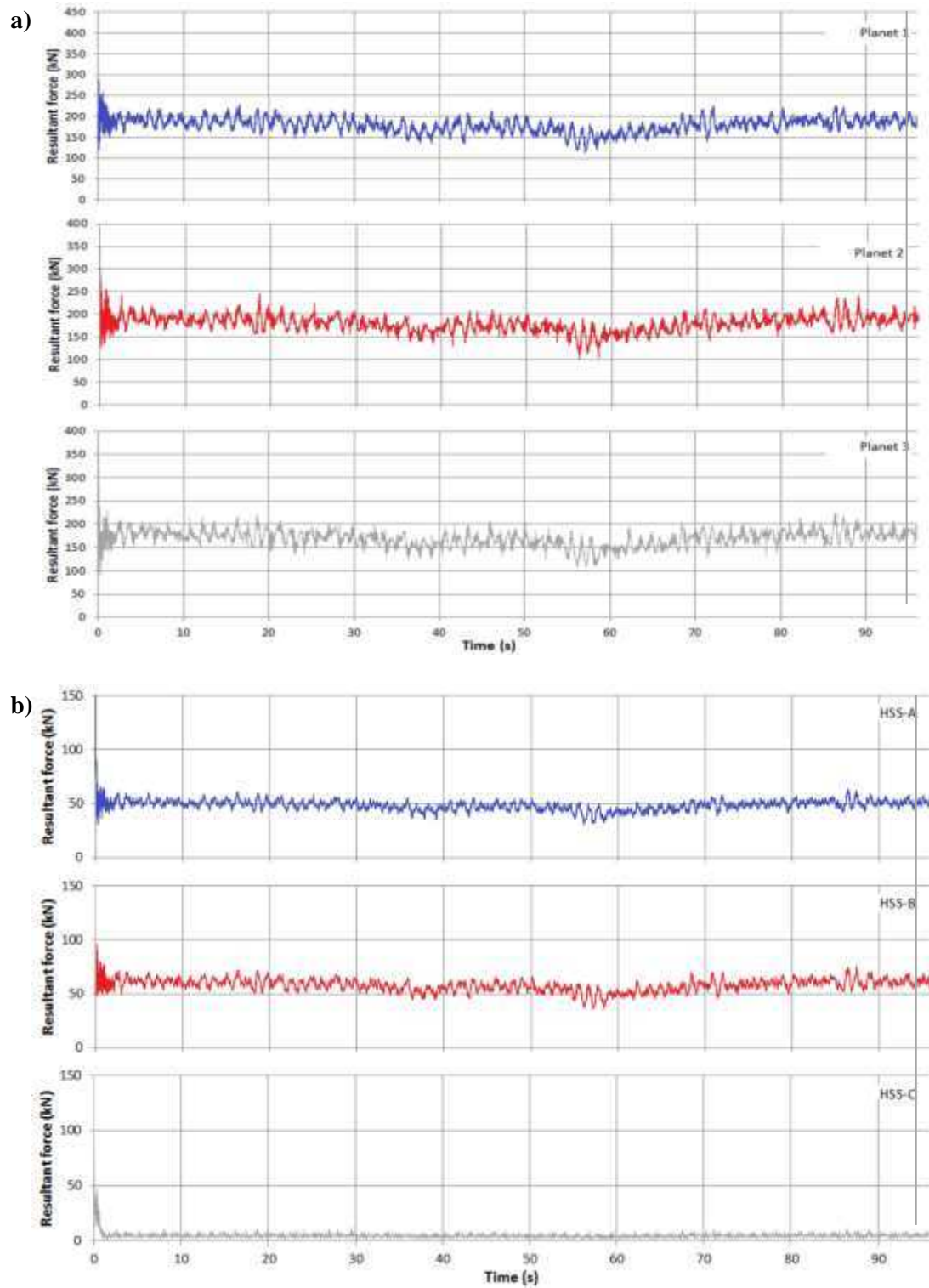
HSS-B and HSS-C respectively.

Figure 6: Resultant forces acting on bearings roller/raceway contacts during normal operation for:
(a) Planetary bearings (b) High speed shaft bearings

5.2. Shut-down

LSS and HSS velocities during shut-down are shown in Figure 7. The simulation was stopped after 36 seconds as rotor velocity was oscillating either side of zero and maximum bearing loading had been experienced. Figure 8a shows that planetary bearing loading peaks after 10 seconds, when the generator is switched offline, then the maximum loading of 358 kN is experienced when the disc brake is engaged at 26 seconds. Figure 8b shows that the HSS bearings experience maximum resultant force magnitudes of 110 kN for HSS-A, 102 kN for HSS-B and 63 kN for HSS-C under braking.
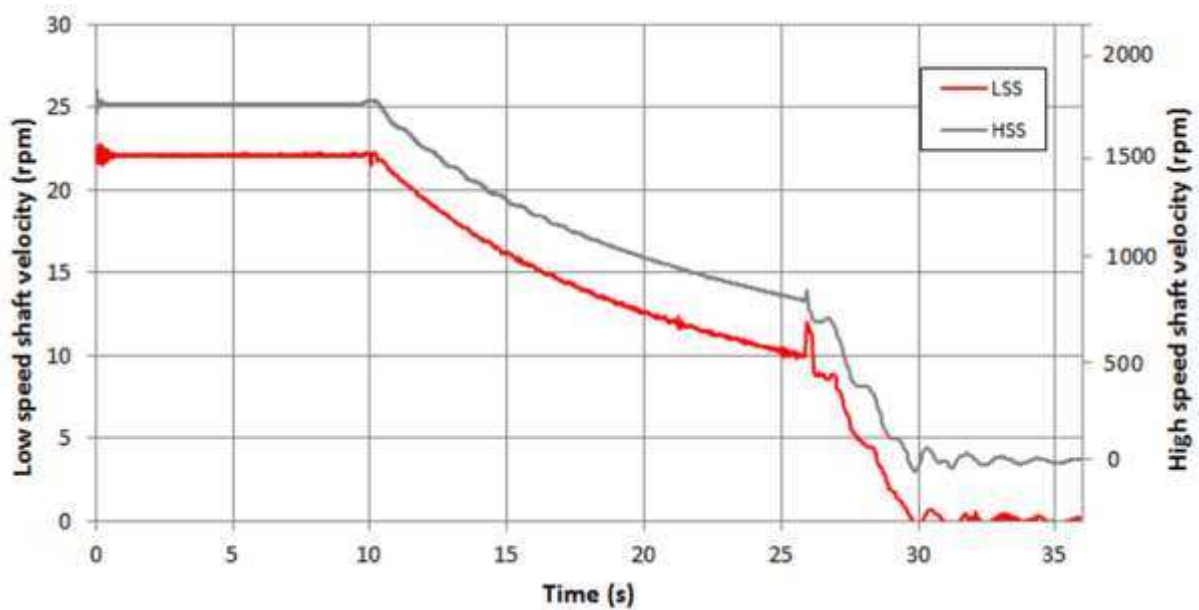
Figure 7: LSS and HSS velocity during shut-down
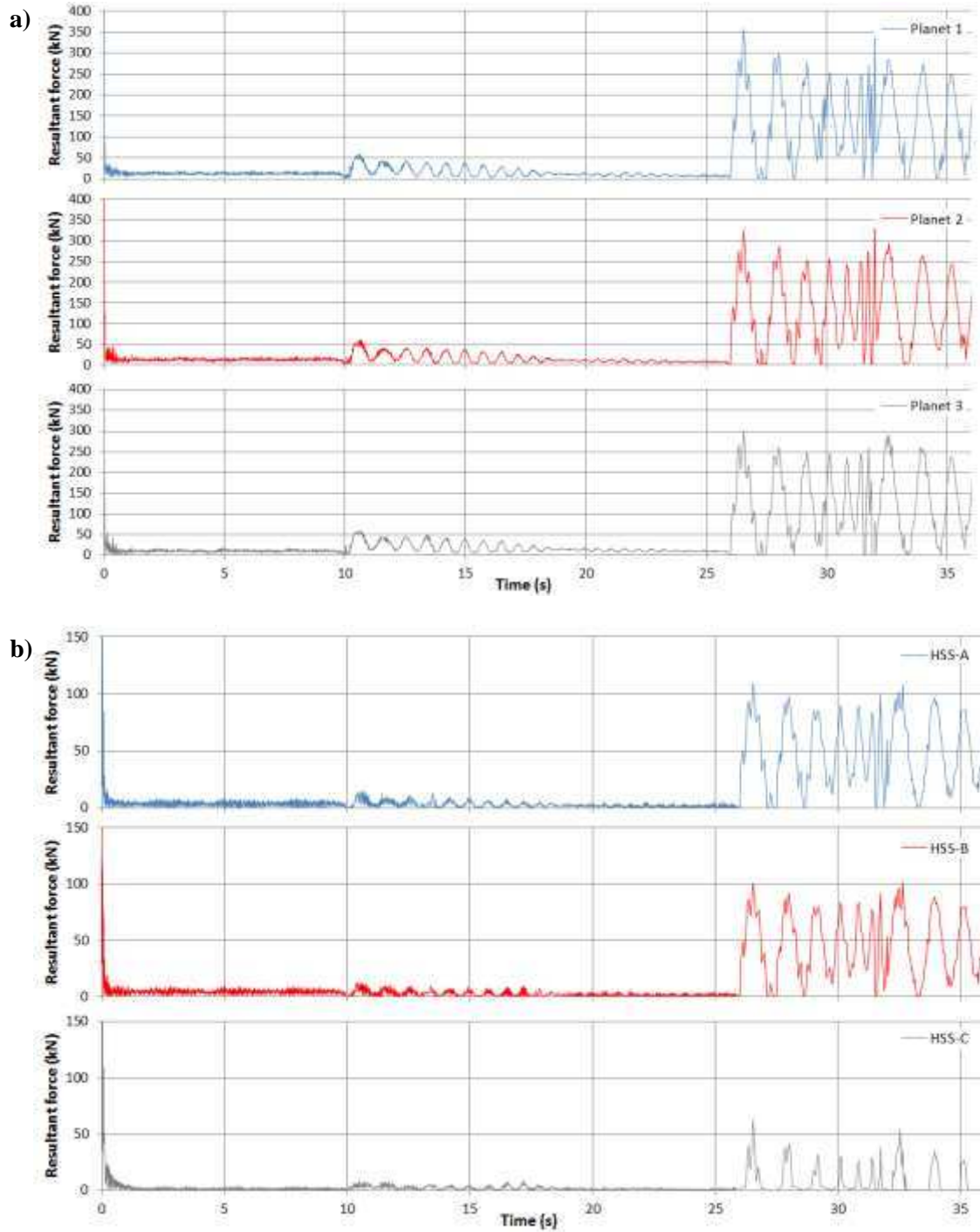
Figure 8: Resultant forces acting on planetary bearings roller/raceway contacts during shut-down for:
(a) Planetary bearings (b) High speed shaft bearings

5.3. Maximum Hertzian contact pressures

Maximum inner race contact pressures were calculated because most WTGBs fail on the inner

race. As previously mentioned, the developed dynamic model in this study has not taken into account

unequal load sharing between the upwind and downwind planetary bearings. Previous studies [29-31]

have found that upwind planetary bearings experience considerably higher loading; up to 1.3 times higher [30]. This factor is taken into account when calculated planetary bearing contact stress.

Tables 2 and 3 show calculated maximum Hertzian stress experienced for normal operation and shut-down respectively. Stresses are presented as a percentage of the maximum allowable contact stress at Miner's sum dynamic equivalent bearing load (P_{max}) as listed in current wind turbine design standards [32]; 1,500 MPa for low speed planetary bearings and 1,300 MPa for HSS bearings.

	PLA	PLB	PLC	HSSA	HSSB	HSSC
P (kN)	277	322	278	63	78	15
p_0 (MPa)	1410	1520	1410	1170	688	305
% of P_{max} reached	94	101	74	90	83	20

Table 2: Maximum bearing contact stresses during normal operation

	PLA	PLB	PLC	HSSA	HSSB	HSSC
P (kN)	412	408	345	110	102	63
p_0 (MPa)	1720	1710	1570	1540	788	618
% of P_{max} reached	115	114	105	118	61	48

Table 3: Maximum bearing contact stresses during shut-down

6. Discussion

A dynamic gearbox model has been created and successfully validated in this study. Bearing loading results can be assumed to be accurate, taking into account the following limitations of the model:

- Inability to model load sharing between planet gear bearing pairs;

- Inability to model off-axis loads (Z′ DOF) from the rotor and generator;

- Inability to model internal component deflections.

It can be seen that planetary loading is fairly evenly shared between the three planetary gears, during both shutdown and normal operation, suggesting that the splined shaft connection does promote load sharing in the planetary stage. Planetary bearings are loaded to higher magnitudes than HSS bearings during both operating regimes, exceeding maximum the recommended contact stress by 15% during shutdown and by 1% during normal operation. Bearing HSSA on the HSS is also loaded to a high percentage of the recommended level during normal operation (90%) and significantly

exceeds it during shutdown (by 18%). It is anticipated that extreme operating conditions, such as emergency shutdown, would further increase contact stresses.

The TRB pair, HSS-B and HSS-C do not come close to exceeding recommended stress levels. This could be because TRBs are designed to withstand high axial loading, which was not experienced during these simulations. Radial loading is shared between the two tapered bearings, whereas axial load is only supported by one of the two, as HSS-B is takes the positive axial load, while HSS-C takes the negative. Loading on HSS-B is considerably higher than HSS-C. This is likely to be because HSS-B takes a greater share of the load in the radial direction, to a greater extent than HSS-C, because it is closer to the meshing gears.

Maximum bearing loading conditions were experienced under braking during manual shutdown, inducing greater transient bearing loading than that during normal operation. The shutdown event also produced large torque reversals in the gearbox, visible by the highly fluctuating bearing loading during braking. This would likely cause hammering impact between the roller and raceway. It is anticipated that during emergency stop events, this will be experienced at higher levels.

Another consideration is that sub-surface material defects in the bearing steel microstructure act as stress raisers [9], locally increasing the stress that the material experiences and likely causing plastic deformation in their close proximity. Further work will be carried out to confirm this and to identify the loading levels at which it occurs.

This paper has assumed that all rolling elements are identically sized, which in reality is not the case and any variation may have large implications on load sharing [33]. Bearing misalignment and resulting roller edge loading has not been considered and would lead to a considerably reduced contact area and therefore a considerably increased contact pressure. As previously mentioned, rollers and raceways have been assumed to be perfect cylinders under ideal Hertzian line contact, which equally distributes loading over the length of the line contact. The small increase in contact pressure caused by roller profiling has not been considered.

This study has shown that under normal operating conditions such as shutdown, the bearing loading exceeds recommended values both on the high speed shaft and the low speed planetary stage, using a simulation method that likely underpredicts contact stresses. During extreme events such as

emergency shutdown or grid disconnection due to grid faults, the bearing loading is very likely to be higher. As a result the bearings used in this gearbox are thought to be undersized and unable to operate at rated torque and during manual shutdown for their design lifetime.

7. Conclusions

A multibody dynamic model of a 750 kW wind turbine gearbox has been successfully developed, validated and used to simulate normal operation and manual shutdown. Bearing loading variations in the time domain have been calculated and analysed. The model found that the gearbox bearings were undersized and recommended contact stresses were exceeded on four of the six analysed bearings:

1. It was found that during normal operation, the maximum contact stress on one of the planetary bearing inner raceways exceeded the maximum recommended level by 1 %.

2. During the braking event in the wind turbine shutdown procedure, contact stresses in the planetary bearings exceeded the maximum recommended level in all bearings and by a maximum of 15% in one of the bearings.

3. The upwind high speed shaft bearing HSS-A, experienced contact stresses 18% higher than recommended levels during manual shutdown.

4. In the NREL 750 kW test wind turbine, gearbox bearings are operating at contact stress levels higher than the recommended values during normal operating conditions and therefore may accumulate fatigue damage when operating at rated torque and when undergoing manual shutdown.

Acknowledgements

References

1. Scott, K., S, Infield, D., Barltrop, N., Coultate and J., Shahaj, A. (2011) Effects of extreme and transient loads on wind turbine drive trains, In: 50th AIAA Aerospace Sciences Meeting Including the New Horizons Forum and Aerospace Exposition. American Institute of Aeronautics and Astronautics.

2. Musial, W., Butterfield, S. and McNiff, B. (2007) Improving wind turbine gearbox reliability, National Renewable Energy Laboratory.

3. Ribrant, J. and Berting, L.M. (2007) Survey of failures in wind power systems with focus on Swedish wind power plants during 1997-2005, Transactions on Energy Conversion, 22(1), 167-173.

4. British Standards Institution (2008) BS ISO 281:2007: Rolling Bearings - Dynamic load ratings and rating life.

5. Tavner, P. J., Xiang, J. and Spinato, F. (2007) Reliability analysis for wind turbines, Wind Energy, 10(1), 1-18.

6. Jain, S. and Hunt, H. (2011) A dynamic model to predict the occurance of skidding in wind turbine gearbox bearings, Journal of Physics, 305(1).

7. Oyague, F., (2009) Gearbox modeling and load simulation of a baseline 750-kW wind turbine using state-of-the-Art simulation codes. Technical Report, National Renewable Energy Laboratory, NREL/TP-500-41160 .

8. Commision of the European Communities (2008) Offshore Wind Energy: Action needed to deliver on the Energy Policy Objectives for 2020 and beyond. Technical Report, COM(2008) 768.

9. Evans, M. H. (2005) White structure flaking (WSF) in wind turbine gearbox bearings: effects of 'butterflies' and white etching cracks (WEC), Materials Science and Technology, 28(1), 3-22.

10. Stadler, K. and Stubenrauch, A. (2013) Premature bearing failures in industrial gearboxes. Technical Repoert, SKF, ATK 2013.

11. SKF Bearings (1994) Bearing failures and their causes. Technical Report, Product information 401.

12. Sankar, S., Nataraj, M. and Raja, V. (2012) Failure analysis of bearing in wind turbine generator gearbox, Journal of Information Systems and Communication, 3(1), 302-309.

13. Rosinski, J. and Smurthwaite, D. (2010)**,** Toubleshooting Wind Gearbox problems. Article, Gear Solutions.

14. Luyckx, J. (2011) WEC failure mode on roller bearings. Presentation at Wind Turbine Tribology Seminar, Hansen Transmissions.

15. Cambell, F. (2008). Elements of Metallurgy and Engineering Alloys. Ohio: ASM International. 243 – 262.

16. Errichello, R., Budny, R. and Eckert, R. (2013) Investigations of bearing failures associated with white etching areas (WEAs) in wind turbine gearboxes, Tribology Transactions, 56(6), 1069-1076.

17. Greco, A., Sheng, S., Keller, J. and Erdemir, A. (2013) Material Wear and Fatigue in Wind Turbine Systmes, Wear, 302(1-2), 1583-1591.

18. Peeters, J. L. M., Vandepitte, D. and Sas, P. (2005) Analysis of Internal Drive Train Dynamics in a Wind Turbine, Wind Energy, 9(1-2), 141-161.

19. Helsen, J., Vanhollebeke, F., Marrant, B., Vandepitte, D. and Desmet, W. (2011) Multibody modelling of verying complexity for model behaviour analysis of wind turbine gearboxes, Renewable Energy, 36(11), 3098-3113.

20. Oyague, F. (2008) Progressive dynamical drive train modeling as part of NREL Gearbox Reliability Collaborative, Technical Report, National Renewable Energy Laboratory, NREL/CP-500-43473.

21. Link, H., LaCava, W., van Dam, J., McNiff, B., Sheng, S., Wallen, R., McDade, M., Lambert, S., Butterfield, S., and Oyague. F. (2011) Gearbox Reliability Collaborative project report: Findings from phase 1 and phase 2 testing. Technical Report, National Renewable Energy Laboratory, NREL/TP-5000-51885.

22. LaCava, W., Guo, Y., Xing, Y., and Moan, T. (2012) Determining wind turbine gearbox model complexity using measurement validation and cost comparison, Conference Paper, National Renewable Energy Laboratory, NREL/CP-5000-54545.

23. Houpert, L. (1997), A uniform analytical approach for ball and roller bearings calculations, Journal of Tribology, 119(4), 851-858.

24. Ricardo PLC (2012), VALDYN User's Manual.

25. SKF (2003) General Catalogue.

26. International Organization for Standardization (2006) ISO 6336-3: Calculation of load capacity of spur and helical gears.

27. NSK (2009) Bearing internal load distribution and displacement. Chapter from Catalogue: Rolling Bearings.

28. Hertz, H. (1881), On the contact of elastic solids, Math, 92, (156–171), Translated and reprinted in English in Hertz's Miscellaneous Papers, Reine Angew, J. (1896) Macmillan & Co., London, UK.

29. Guo, Y., Keller, J. and LaCava, W. (2012) Combined effects of gravity, bending moment, bearing clearance, and input torque on wind turbine planetary gear load sharing. Conference Paper, National Renewable Energy Laboratory, NREL/CP-5000-55968.

30. Lacava, W., Keller, J, Mcniff, B. (2012) Gearbox Reliability Collaborative: Test and model investigation of sun orbit and planet load share in a wind turbine gearbox, Conference Paper, National Renewable Energy Laboratory, NREL/CP-5000-54618.

31. Lacava, W., Xing, Y., Marks, C., Guo, Y. and Moan, T. (2013) Three-dimensional bearing load share behavior in the planetary stage of a wind turbine gearbox, IET Renewable power Generation, 7(4), 1752-1416.

32. International Organisation for Standardization (2012) IEC 61400-4:2012: Wind turbines -- Part 4: Design requirements for wind turbine gearboxes.

33. Yu, S., Wang, D., Dong, H. and Wang, B. (2013) A New Method for Determining Load Distributions among Rollers of Bearing with Manufacturing Errors, Journal of Mechanical Engineering Science, 227(11), 2402-2415.

Appendix

Rotor	Planet carrier	Gears (All gears)	Shafts (All shafts)	Bearings (All bearings)	Brake	Casing	Generator
Mass	Dimensions	No. of teeth	Dimensions	Axial damping	Peak normal force	Mass and inertia (6 DOF)	Mass and inertia of generator rotor (6 DOF)
Moment of inertia (z')	Mass and inertia (6 DOF)	Gear module	Young's modulus	Radial damping	Inner radius of disc contact area	Casing dimensions	
		Addendum modification	Shear modulus	Tilt damping	Outer radius of disc contact area	Elastomer mount stiffness (6 DOF)	
		Normal pressure angle	Mass and inertia (6 DOF)	Coefficient of rotational friction			
		Helix angle	Spline dimensions	Number of rolling elements	Static friction coefficient	Elastomer mount damping (6 DOF)	
		TIF diameter	Bending damping about X	Rolling element diameter	Coulomb friction coefficient		
		Tip diameter	Bending damping about Y	Bearing bore diameter			
		Tooth face width		Bearing outer diameter	Stribeck velocity		
		Normal backlash allowance	Axial damping	Rolling element contact length	Mass of brake disc		
		Contact stiffness	Torsional damping	Contact angle			
		Damping coefficient					
		Friction coefficient					
		Mass and inertia (6 DOF)					

Table 4: Required parameters to create the gearbox model